



**HAL**  
open science

## Mapping and interpretation of Sinlap crater on Titan using Cassini VIMS and RADAR data

Stéphane Le Mouélic, Philippe Paillou, Michael Janssen, Jason Barnes,  
Sébastien Rodriguez, Christophe Sotin, Robert Brown, Kevin Baines, Bonnie  
Buratti, Roger Clark, et al.

### ► To cite this version:

Stéphane Le Mouélic, Philippe Paillou, Michael Janssen, Jason Barnes, Sébastien Rodriguez, et al.. Mapping and interpretation of Sinlap crater on Titan using Cassini VIMS and RADAR data. *Journal of Geophysical Research. Planets*, 2008, 113 (E4), pp.E04003. 10.1029/2007je002965 . hal-03657639

**HAL Id: hal-03657639**

**<https://u-paris.hal.science/hal-03657639>**

Submitted on 3 May 2022

**HAL** is a multi-disciplinary open access archive for the deposit and dissemination of scientific research documents, whether they are published or not. The documents may come from teaching and research institutions in France or abroad, or from public or private research centers.

L'archive ouverte pluridisciplinaire **HAL**, est destinée au dépôt et à la diffusion de documents scientifiques de niveau recherche, publiés ou non, émanant des établissements d'enseignement et de recherche français ou étrangers, des laboratoires publics ou privés.

Copyright



## Mapping and interpretation of Sinlap crater on Titan using Cassini VIMS and RADAR data

Stéphane Le Mouélic,<sup>1,2</sup> Philippe Paillou,<sup>3</sup> Michael A. Janssen,<sup>4</sup> Jason W. Barnes,<sup>5</sup> Sébastien Rodriguez,<sup>6</sup> Christophe Sotin,<sup>1,4</sup> Robert H. Brown,<sup>7</sup> Kevin H. Baines,<sup>4</sup> Bonnie J. Buratti,<sup>4</sup> Roger N. Clark,<sup>8</sup> Marc Crapeau,<sup>3</sup> Pierre J. Encrenaz,<sup>9</sup> Ralf Jaumann,<sup>10</sup> Dirk Geudtner,<sup>11</sup> Flora Paganelli,<sup>4</sup> Laurence Soderblom,<sup>12</sup> Gabriel Tobie,<sup>1,2</sup> and Steve Wall<sup>4</sup>

Received 12 July 2007; revised 28 September 2007; accepted 4 December 2007; published 12 April 2008.

[1] Only a few impact craters have been unambiguously detected on Titan by the Cassini-Huygens mission. Among these, Sinlap is the only one that has been observed both by the RADAR and VIMS instruments. This paper describes observations at centimeter and infrared wavelengths which provide complementary information about the composition, topography, and surface roughness. Several units appear in VIMS false color composites of band ratios in the Sinlap area, suggesting compositional heterogeneities. A bright pixel possibly related to a central peak does not show significant spectral variations, indicating either that the impact site was vertically homogeneous, or that this area has been recovered by homogeneous deposits. Both VIMS ratio images and dielectric constant measurements suggest the presence of an area enriched in water ice around the main ejecta blanket. Since the Ku-band SAR may see subsurface structures at the meter scale, the difference between infrared and SAR observations can be explained by the presence of a thin layer transparent to the radar. An analogy with terrestrial craters in Libya supports this interpretation. Finally, a tentative model describes the geological history of this area prior, during, and after the impact. It involves mainly the creation of ballistic ejecta and an expanding plume of vapor triggered by the impact, followed by the redeposition of icy spherules recondensed from this vapor plume blown downwind. Subsequent evolution is then driven by erosional processes and aeolian deposition.

**Citation:** Le Mouélic, S., et al. (2008), Mapping and interpretation of Sinlap crater on Titan using Cassini VIMS and RADAR data, *J. Geophys. Res.*, 113, E04003, doi:10.1029/2007JE002965.

### 1. Introduction

[2] Titan is the only satellite in the solar system to have a dense atmosphere, which is composed primarily of nitrogen with few percent of methane. This atmosphere is completely

opaque at visible wavelengths, due to the absorption of aerosols and gas and scattering by aerosols.

[3] Three instruments onboard the Cassini spacecraft can be used to see through the haze. The ISS camera [Porco *et al.*, 2005] provides images of the surface in the 0.93- $\mu\text{m}$  filter, once the strong scattering by aerosols has been corrected by image enhancement techniques [Perry *et al.*, 2005]. The Visual and Infrared Mapping Spectrometer (VIMS) acquires hyperspectral images in 352 contiguous spectral channels between 0.3 and 5.2  $\mu\text{m}$  [Brown *et al.*, 2003, 2004]. VIMS provides information about the morphology of the surface thanks to seven infrared windows, where the atmospheric methane does not absorb [Sotin *et al.*, 2005]. In particular, very sharp images are acquired at 2  $\mu\text{m}$ , where the scattering by aerosols is much reduced compared to the visible wavelengths. The spectral dimension of the VIMS data set can be used to check for compositional variations within a given scene. Finally, the Cassini RADAR is composed of four instruments: the imaging Synthetic Aperture Radar (SAR), the altimeter, the passive radiometer and the scatterometer. The RADAR instruments operates in Ku-band (13.78 GHz, 2.18 cm

<sup>1</sup>Université de Nantes, Laboratoire de Planétologie et Géodynamique, Nantes Cedex 03, France.

<sup>2</sup>CNRS, UMR-6112, Nantes Cedex 03, France.

<sup>3</sup>Observatoire Aquitain des Sciences de l'Univers-UMR 5804, Floirac, France.

<sup>4</sup>Jet Propulsion Laboratory, Pasadena, California, USA.

<sup>5</sup>NASA Ames Research Center, Moffett Field, California, USA.

<sup>6</sup>Université Paris 7, Laboratoire AIM, Centre d'étude de Saclay, DAPNIA/Sap, Centre de l'Orme des Merisiers, France.

<sup>7</sup>Lunar and Planetary Lab, University of Arizona, Tucson, Arizona, USA.

<sup>8</sup>USGS, Denver, Colorado, USA.

<sup>9</sup>Observatoire de Paris/Université Pierre et Marie Curie, Paris, France.

<sup>10</sup>DLR, Institute for Planetary Research, Berlin, Germany.

<sup>11</sup>German Aerospace Center, Microwave and Radar Institute, Germany/Canadian Space Agency, Spacecraft Payloads, Canada.

<sup>12</sup>USGS, Flagstaff, Arizona, USA.

wavelength), and therefore the propagation of the radar wave is unaffected by the atmosphere [Elachi *et al.*, 2006].

[4] Cross comparison between ISS, VIMS and RADAR images have been undertaken in order to understand various regions with as much data as possible. Global VIMS and RADAR data comparisons have been made in order to check for systematic correlation related to surface properties [Soderblom *et al.*, 2007; Barnes *et al.*, 2007]. Soderblom *et al.* [2007] found that dune fields seen in SAR images are generally correlated with VIMS “dark brown” units in RGB color composites made from the 2.0- $\mu\text{m}$ , 1.6- $\mu\text{m}$  and 1.3- $\mu\text{m}$  images. However, the correlation between the two data sets is not systematic. The absence of correlation between RADAR and VIMS bright units, observed in particular on the Huygens landing site (observed by both instruments, with a 15 km/pixel resolution by VIMS), was interpreted as the result of an optically thick bright mantling which might be transparent to the radar. Barnes *et al.* [2007] investigated the relationships between VIMS and RADAR imagery on an equatorial region east of Xanadu using data from the ninth flyby (T9 on 26 December 2005) and eighth flyby (T8 on 28 October 2005) respectively. Channels have been observed in the two data sets, showing that VIMS was able to detect channel materials despite sub-pixel channel widths. It was also concluded that the dark materials in VIMS, which were usually considered to be topographically lower than bright materials, correspond in this particular case to mountain ranges detected by the radar.

[5] In this paper, we focus on the Sinlap crater, which is one of the very few impact craters that has been confidently identified on Titan during the first 30 flybys [Lorenz *et al.*, 2007]. Impact craters are particularly interesting as they provide a window into the crust by excavating materials from beneath the surface. Sinlap is located at 16°W, 11°N. It has been observed once by the RADAR instrument during the third flyby (T3 on 15 February 2005) and twice by VIMS with a medium resolution during the first two years of the Cassini mission.

[6] We concentrate in particular on the complementarity between VIMS and RADAR (SAR and passive radiometry) observations in order to investigate the compositional diversity of this particular area. First, we describe the different processing steps we apply to VIMS data in order to enhance both their spatial and spectral information content. Then we compare the heterogeneity maps derived from the infrared hyperspectral measurements with the SAR imagery acquired over the Sinlap crater area. We give an interpretation of the observed correlations (and absences of correlation), taking an Earth analog as a comparison. We show that areas which are consistent with a local enrichment in water ice according to VIMS correlate with a significant increase in dielectric constant derived from polarized radiometric measurements, which is also consistent with a higher water ice content than the surroundings. Finally, a possible geologic history of the Sinlap crater concludes this paper.

## 2. Processing of VIMS Images

[7] Sinlap crater has been observed twice by VIMS. The first observation was obtained during T5 flyby on 16 April 2005 with a resolution of 18 km/pixel (cube CM\_1492364864, acquired with a phase angle of 56–58°, an incidence angle

from 63° to 84°, an emergence angle from 4° to 37°, and an exposure time of 80 ms). The second observation of Sinlap by VIMS was obtained during T13 flyby on 30 April 2006 with a resolution of 14 km/pixel (cube CM\_1525118253\_1.cub, with a phase angle ranging between 40° and 42°, an incidence angle varying between 30° and 47°, an emergence angle from 0° to 20°, and an exposure time of 68 ms). These second observing conditions are therefore the best achieved so far by VIMS in this area, considering the fact that high solar incidence angles ( $>\sim 70^\circ$ ) often lead to strong spurious atmospheric effects.

### 2.1. Enhancement of Spatial Features

[8] Before discussing the spectral characteristics of the VIMS data, it is important to state how the raw VIMS images can be processed in order to improve their spatial mapping capabilities. It has already been noted that the surface can be seen in seven spectral windows in the infrared [Sotin *et al.*, 2005; Rodriguez *et al.*, 2006; Barnes *et al.*, 2006a, 2006b; McCord *et al.*, 2006]. The best images in terms of contrast are acquired in the 2- $\mu\text{m}$  window, where the signal from the surface is sufficiently strong while the scattering by the atmosphere (a blurring effect decreasing with increasing wavelength) is already low enough. Five spectral channels can be used in the 2- $\mu\text{m}$  window to see the surface. When no spectral information is needed, we can then co-add several channels within the methane transmission windows in order to increase the signal-to-noise ratio of the images. This is particularly useful for low time exposure acquisitions (such as the 13 ms ones used during the T20 flyby at closest approach, e.g., Le Mouélic *et al.* [2007]). For improving the image sharpness that emphasized surface features, best results are obtained by: 1) adding up to 12 spectral channels in the 7 methane windows; 2)- oversampling the actual cube resolution by a factor of four, 3)- applying a bilinear interpolation to smooth the pixels, 4)- applying an unsharp mask procedure. This unsharp mask procedure is similar to the one used for ISS images [Perry *et al.*, 2005]. It simply consists in subtracting  $\sim 60\%$  of a low-pass filtered image. An example of this processing pipeline is given in Figure 1 on the T13 Sinlap cube. It should be noted that this strategy is very useful for geomorphological analyses, but the final unsharp mask procedure should not be used prior to spectral analyses as it may modify the spectra.

### 2.2. Analysis of Band Ratios

[9] In order to emphasize subtle spectral variations in the Sinlap area, we use the band ratio technique. Band ratios are useful to cancel out the effects of albedo and illuminating conditions, therefore highlighting subtle spectral differences. Figure 2a shows a mosaic at 2.03  $\mu\text{m}$  of the T5 cube CM\_1492364864 overlying the two adjacent cubes labeled CM\_1492364272\_1.cub and CM\_1492363683\_1.cub. The most relevant ratio images of the T5 flyby are presented in Figures 2b to 2e. The 2.03- $\mu\text{m}$  image (Figure 2a) shows mainly dark materials within the crater floor, as delineated in the RADAR image, surrounded by a ring of bright materials (named Bazaruto Facula), possibly related to the main ejecta blanket. We did not retrieve other significant information from this and other single band images.

[10] The 2.03/1.27- $\mu\text{m}$  and 1.59/1.27- $\mu\text{m}$  ratio images (Figures 2b and 2c) reveal a spectrally distinct unit (appear-

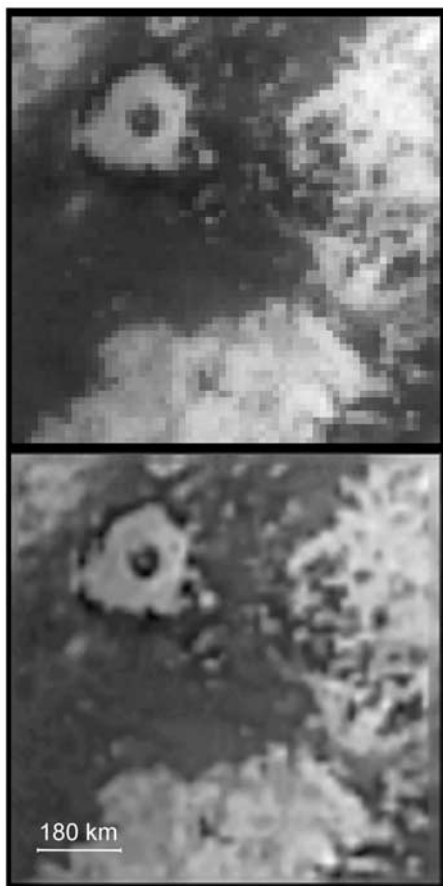


**Figure 1.** Enhancement of surface features. Top: raw VIMS channel at  $2.03 \mu\text{m}$ . Bottom: same after co-addition of 12 channels within methane windows, oversampling, bilinear interpolation and unsharp mask procedure. The circular bright feature is named Bazaruto Facula, which surrounds Sinlap crater.

ing dark) surrounding the main bright ejecta blanket. This unit appears with low values in both ratios, but does not show up in the  $1.27/1.08\text{-}\mu\text{m}$  ratio (Figure 2e). This spectral behavior is similar to the one observed north of the Huygens landing site by *Rodriguez et al.* [2006]. It also corresponds to the so-called “dark blue” materials seen in the work of *Barnes et al.* [2006b] and *Soderblom et al.* [2007]. It can be explained by a local enrichment in water ice, which displays two deep absorption bands at  $1.6$  and  $2.0 \mu\text{m}$  and a relatively high reflectance in the  $1.27$  and  $1.08\text{-}\mu\text{m}$  windows [e.g., *Rodriguez et al.*, 2006, Figure 10]. No spatial variation is observed in the  $2.69/2.78\text{-}\mu\text{m}$  ratio (no surface feature appears above the noise level in Figure 2d), which indicates that the corresponding material is not made of pure fine-grained water ice only, which would be characterized by a strong decrease in reflectance between  $2.69$  and  $2.78 \mu\text{m}$ . Figure 2f corresponds to a false color composite with the red channel controlled by the  $1.59/1.27\text{-}\mu\text{m}$  ratio, the green channel controlled by the  $2.03/1.27\text{-}\mu\text{m}$  ratio and the blue channel controlled by the  $1.27/1.08\text{-}\mu\text{m}$  ratio. This color coding presents an alternative to the false color coding used by *Barnes et al.* [2006b], where the red, green and blue

channels are respectively controlled by the  $5\text{-}\mu\text{m}$ ,  $2\text{-}\mu\text{m}$ , and  $1.3\text{-}\mu\text{m}$  images, and to the one used by *Soderblom et al.* [2007], which was based on  $2\text{-}\mu\text{m}$ ,  $1.59\text{-}\mu\text{m}$  and  $1.3\text{-}\mu\text{m}$  channels. This false color composite computed from band ratios generally shows more color diversity than the false color composites produced from single bands only.

[11] The second observation of Sinlap during the T13 flyby (cube labeled CM\_1525118253\_1) was obtained with a much more favorable viewing geometry than during the T5 flyby, with an incidence angle less than  $47^\circ$ . It is particularly interesting to see that the ratio images performed with T13 data (see Figure 3) show the same spectral units as the one observed more than one year earlier at T5. No significant change is observed between the T5 and T13 observations at this spatial resolution. This indicates that the observed variations are linked to the surface and not due to transient atmospheric phenomena. Because of the lower incidence and phase angles (and therefore lower atmospheric blurring), the band ratios also appear sharper than at T5. The color composite derived from band ratios (bottom right of Figure 3) reveals the spectral heterogeneity of the Sinlap area. In this color-coding choice, areas possibly enriched in water ice appear blue to dark blue around the main bright circular ejecta of the crater, and other low albedo regions appear brown, with small shades of red.

### 2.3. First Order Correction of the Aerosols Additive Scattering

[12] It can be argued that the scattering by the atmosphere, acting as a global additive effect depending on the wavelength, may affect the band ratios, inducing a dependence on the albedo. This issue has already been raised by *Rodriguez et al.* [2006]. In order to test the stability of the observed surface features in false color images, we therefore computed new ratios using data corrected from the additive component using the first order radiative transfer model presented by *Rodriguez et al.* [2006]. This model is only taking into account the scattering by spherical aerosols, and does not include the transmission of atmospheric gas. For this test, we used a layer of  $200 \text{ km}$  of aerosols, with a concentration of  $100$  particles per  $\text{cm}^3$ , a mean radius of  $0.165 \mu\text{m}$  and an asymmetry factor  $g = 0.4$ . The corresponding new color ratio composite is shown in Figure 4, with the same color-coding as the one used in Figure 3.

[13] We can see that this correction process emphasizes the spectral variations detected in the false color composite. However, it does not change markedly the interpretation of the ratios computed without this correction, and the main unit which shows up in the image is again the bluish to dark area with a parabolic shape surrounding the bright annulus of the crater (Bazaruto Facula). A single pixel, which will be discussed in the next section, also appears in green south of Sinlap.

### 2.4. Analysis of the Spectra

[14] Figure 5 shows the VIMS spectra of the most diverse areas around Sinlap detected by the band ratio analysis at T13. Only a few spectral variations have been observed so far on Titan in the methane windows. Those are: a global change of the overall I/F level within the windows [*Sotin et al.*, 2005; *Rodriguez et al.*, 2006; *McCord et al.*, 2006], changes in restricted areas with high flux at  $5 \mu\text{m}$  such as

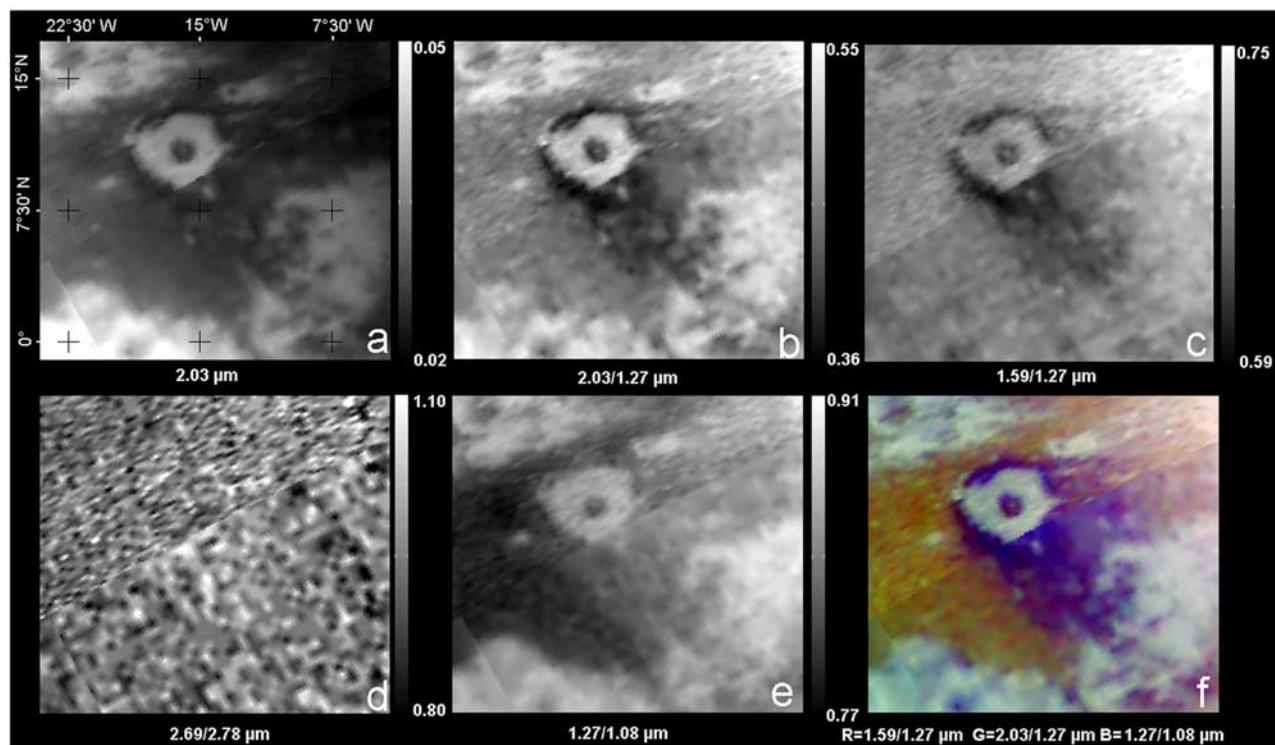


**Figure 2.** VIMS T5 (16 April 2005) observations of Sinlap, acquired with a spatial resolution of 18 km/pixels and a solar incidence angle from  $63^\circ$  to  $84^\circ$ . (a) 2.03- $\mu\text{m}$  image, with I/F values ranging from 0.02 to 0.05. (b) to (e): Band ratios. (f): False RGB color composite of band ratios. Sinlap appears as a bright annulus surrounded by an area absorbing at 1.59 and 2.0  $\mu\text{m}$  (but not at 1.08 and 1.27  $\mu\text{m}$ ), with a parabolic shape oriented toward the South East.

Hotei Regio and Tui Regio [Barnes *et al.*, 2005, 2006a], and areas described as “dark blue” by Barnes *et al.* [2006b, 2007] and Soderblom *et al.* [2007]. Figure 5 displays a series of spectra representative of the diversity of the Sinlap area. This spectra have been extracted from a single observation (T13 cube labeled CM\_1525118253\_1), with very similar observing conditions (therefore minimizing possible differences due to atmospheric effects). We see that several spectra cross each other in the methane windows, which indicates that surface compositional (or physical state) changes do occur in this area.

[15] The red and black spectra in Figure 5 are typical of Titan equatorial bright regions. They differ only by their overall I/F level in each methane window, which seems to indicate that the constituting materials are the same. Green and blue spectra have the same level in the 1.08 and 1.27- $\mu\text{m}$  windows, but differ markedly in the 1.59- $\mu\text{m}$  and 2.03- $\mu\text{m}$  windows. The spectral characteristics of the blue spectrum can be explained by a local enrichment in water ice compared with the surroundings, represented by the purple spectrum taken in the brown unit [Rodriguez *et al.*, 2006; Soderblom *et al.*, 2007]. The green spectrum has a significantly higher I/F value in the 2- $\mu\text{m}$  window. It should be noted that this spectrum is found spatially on a single pixel. A given pixel can be affected by a spike due to a cosmic ray, making the interpretation of single isolated pixels quite spurious. However, it should be noted that this area also appears anomalous (with a slightly higher I/F value at 2  $\mu\text{m}$ ),

again on a single pixel, in the T5 ratio images acquired more than one year earlier. In addition, it does not correspond to a spike in the spectral domain as the whole 2- $\mu\text{m}$  window (covered by 5 different spectels) displays a higher flux. This coincidence is striking enough to think that it might really correspond to a true surface heterogeneity and not to a spike. It should be kept in mind that at the considered spatial resolution ( $\sim 14$  km), small geological features which are possibly different in composition are not resolved. A higher spatial resolution would be needed in order to go deeper into the analysis of this localized anomaly. The main unit which therefore confidently shows up in this analysis corresponds to the dark absorbing materials surrounding the crater, and which spectral characteristics can be explained by a local enrichment in water ice. The areas detected by the analysis of VIMS spectral images will now be compared with the SAR and scatterometer data, in order to look for the correlation between both data sets.

### 3. Radar SAR Images of Sinlap

[16] Sinlap has been observed by the Ku-band (2.17 cm) RADAR instrument in SAR mode during the T3 flyby on 15 February 2005 [Elachi *et al.*, 2006]. A SAR image represents an intensity map of the radar reflectivity of the imaged area (Figure 6). The strength of the returned radar echoes is strongly related to morphological (i.e., surface and near-surface roughness, slope) and electrical (i.e., dielectric

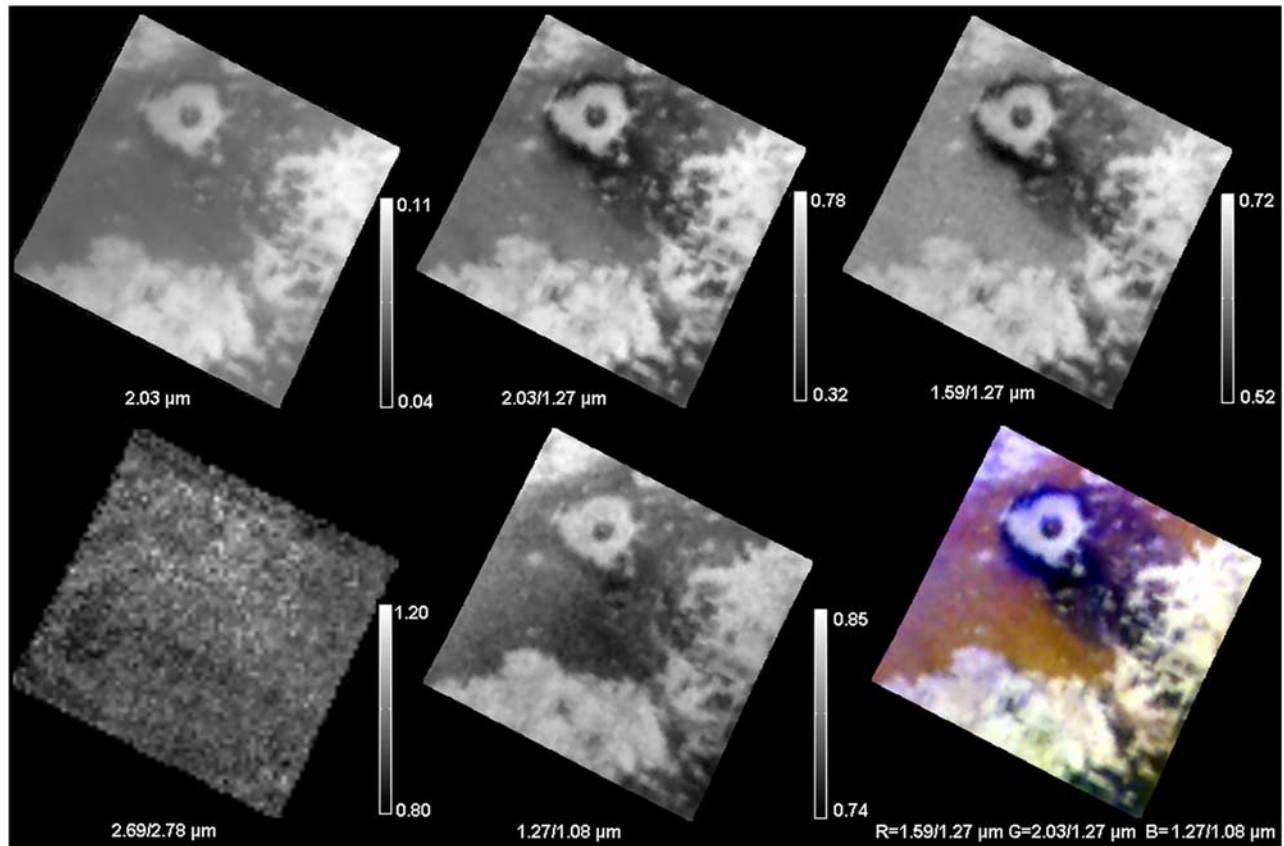


**Figure 3.** 2.03- $\mu\text{m}$  image and band ratios computed from the VIMS T13 (30 April 2006) data, acquired with a resolution of 14 km/pixel and a solar incidence angle of  $30^\circ$  to  $47^\circ$ . The same spatial heterogeneities are observed as in the T5 images acquired one year before (see Figure 2). Materials absorbing at 1.59 and 2.03  $\mu\text{m}$  are again observed around the bright ejecta pattern of the crater.

constant, absorption) characteristics of the surface. In Figure 6, the SAR image shows a flat crater floor, with a 2-km bright spot located west of the crater center. The main rim of the crater appears clearly due to its slopes. *Elachi et al.* [2006] estimated by radarclinometry a wall slope of  $16 \pm 5^\circ$  and a crater depth of  $1300 \pm 200$  m.

[17] The crater is surrounded by a blanket of material having high radar backscatter intensity, possibly ejecta related to the impact process. Careful observation of this blanket shows that it is sub-divided into an internal darker annulus, extending 60 km from the crater rim, and a brighter external zone. The darker annulus around Sinlap rim corresponds to a backscattered power of 0.7 dB, while the outer brighter region corresponds to 2.4 dB, for an incidence angle varying from 12 to 18 degrees over the scene. The darker annulus corresponds to the bright circular area observed in VIMS infrared images (see the white line in Figure 6). The radar-bright materials are surrounded at their western edge by dunes fields [*Lorenz et al.*, 2006]. Such dunes have been observed across Titan at low latitudes and their general trend is eastward, a general orientation that is borne out in recent global circulation models [e.g., *Rannou et al.*, 2006]. One can observe on Figure 6 that dune fields are influenced by the crater topography: the eastern oriented

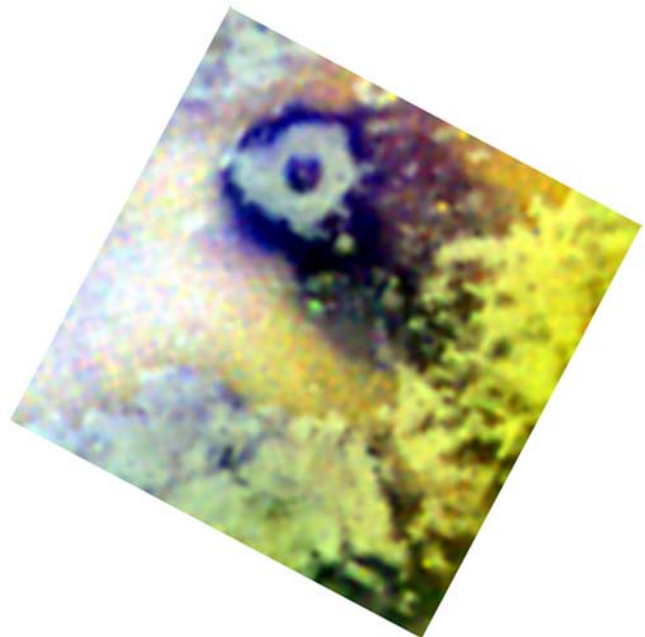


**Figure 4.** RGB false color composite computed from VIMS T13 band ratios corrected from the aerosol scattering using the first order radiative transfert model presented by *Rodriguez et al.* [2006].

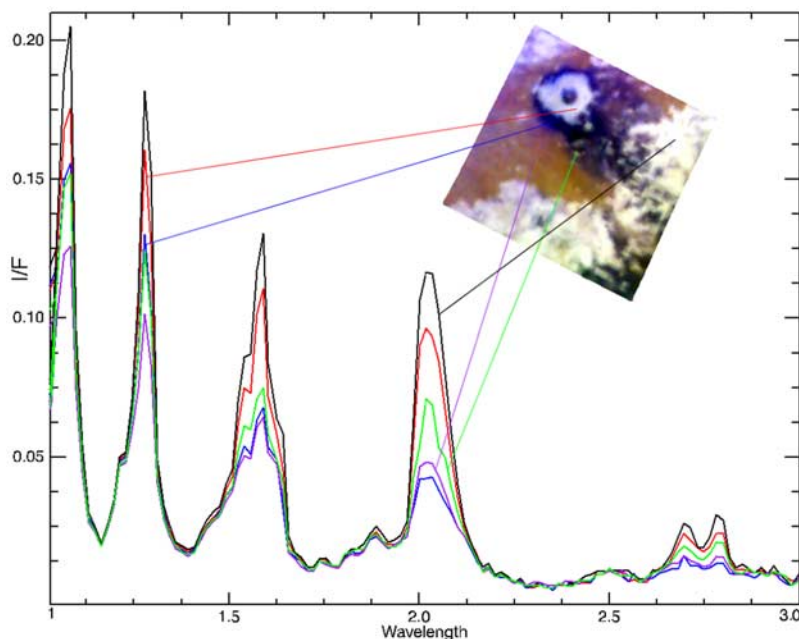


**Figure 5.** Spectral diversity in the Sinlap area, extracted from a single observation (T13 cube labeled CM\_1525118253\_1), therefore with similar viewing geometries. Spectra are crossing each other in the methane windows, indicating compositional variability. The dark blue unit can be explained by a local enrichment in water ice compared to the surroundings.

dunes break around the western crater ejecta border, indicating that the sand flows around the obstacle.

#### 4. Joint Interpretation of VIMS/SAR Data

[18] Combining radar and infrared images leads to the addition of information on the surface geology. Comparing Figures 4 and 6 shows that some VIMS units are correlated to RADAR ones (e.g., crater depression), whereas others are not, like the extent of the ejecta blanket. In this chapter, a detailed description of three areas is performed. First (4.1), differences in the ejecta blanket are described and interpreted as the result of a thin deposit. Second (4.2), the presence of a central peak is discussed. Third (4.3), a spectrally distinct unit South of Sinlap is described. These observations constrain a tentative model of the geological evolution of the Sinlap area during and after the impact (section 6).

##### 4.1. Thin Deposit

[19] The Ku-SAR image shows structures characterized by surface roughness and also reveal structures which are covered by tens of cm-thick aeolian deposits [e.g., Paillou *et al.*, 2006], whereas VIMS is only sensitive to the first tens of microns of Titan's surface. In addition, a thin layer of material might enhance the radar return by lowering the incidence angle, as described on Earth by Elachi *et al.* [1984]. Paillou *et al.* [2006] showed how a two-layer scenario could explain radar bright regions in the Ta flyby RADAR data. A brightening from 0.7 to 2.4 dB as discussed previously can be explained by a 10 cm-thick smooth layer of tholin-like materials covering a rough substratum at the bottom of the external crater wall, according to the electromagnetic modeling described by Paillou *et*

*al.* [2006]. This may account for the observed differences between VIMS and SAR images. The “ejecta blanket” (bright annulus) observed in VIMS images is more or less symmetrical (Figure 4) while it continues asymmetrically to the east in the SAR image (Figure 6). VIMS might observe a flat, superficial deposit of fine-grained materials around Sinlap that only allows the highest part of the rather circular ejecta blanket to outcrop through. In the SAR image, sand dunes located to the west are too thick to let the radar “see” any possible underlying ejecta blanket extending to the west. On the other hand, non-dune aeolian deposits, corresponding to the finest fraction of the sand (and therefore the lightest particles) transported by winds upon the crater rims to the eastern part of the ejecta blanket, could be thin enough (few centimeters) to simultaneously be opaque for VIMS and allow RADAR penetration of the corresponding surface layer to reveal impact ejecta deposits. Turbulences due to small topography variations may hamper the formation of well developed dune fields in the trailing of the crater. In addition, particles may be too small for saltation. A sketch of the proposed surface/subsurface scenario is shown in Figure 7.

[20] The parabolic shape of the bluish areas in the VIMS color ratio composite is aligned with the dunes. It might therefore be related to the wind. It could also explain why we are seeing such bluish areas only on the southern border of the so-called Aztlán equatorial region and not on the northern one.

[21] In order to illustrate the proposed data analysis, we present a terrestrial analogue site in Figure 8. It is an arid area located in southern Libya, mostly covered by a flat aeolian sand sheet. The top part of Figure 8 is an extract of a Landsat ETM image (IR wavelength at 2.2  $\mu\text{m}$ ) showing a flat sandy area with an outcropping low relief of sandstone

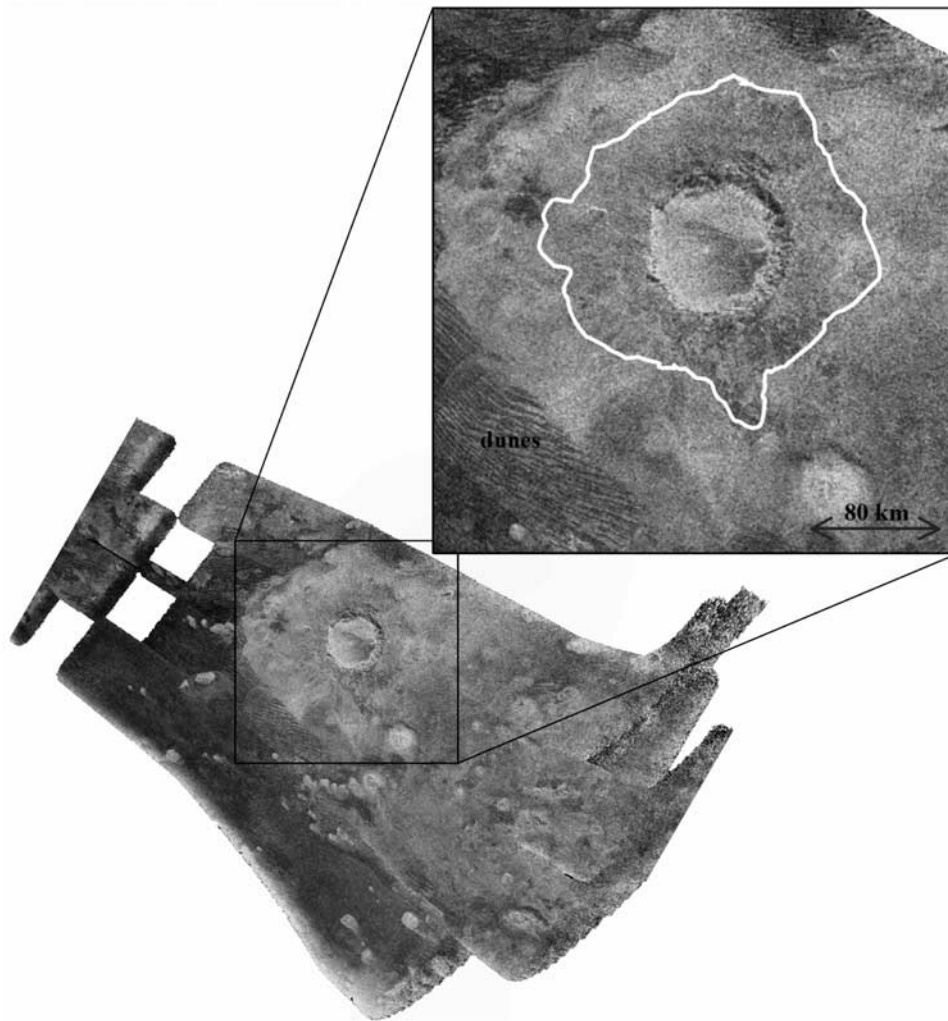


**Figure 6.** SAR image of Sinlap acquired at T3 on 15 February 2005 and zoom of the crater structure. The white line corresponds to the location of a slightly darker (in radar) area on the external part of the crater wall, with a mean backscatter power of 0.7 dB for an incidence angle varying from 12 to 18 degrees over the scene. It also corresponds to the limits of the bright “ejecta” in VIMS images. The outer radar bright region has a mean backscatter power of 2.4 dB. The SAR image covers an area of  $\sim 1000 \times 700$  km.

in which the remains of a double impact crater can be observed [Paillou *et al.*, 2003]. The bottom part of Figure 8 shows the corresponding X-band (9.6 GHz) SAR image acquired by the X-SAR system during the 1994 Shuttle Imaging Radar (SIR-C/X-SAR) mission. In this SAR image, sand dunes appear as dark structures due to the absorption of the radar wave, while the outcropping sandstone appears bright because of its surface roughness (small rocks). The right hand side of the X-band image reveals some subsurface structures (near the impact craters), which are covered by the meter-thick flat sand sheet. Whereas the Landsat image shows an homogeneous sandy surface surrounding the outcropping low relief, the SAR image presents various and rich structures due to the subsurface imaging capabilities of radar. This might be very similar to what Cassini VIMS and RADAR instruments show us around Sinlap crater.

#### 4.2. The Central Peak

[22] Elachi *et al.* [2006] do not report a central peak in Sinlap, which seems to have a flat floor in the RADAR image. However, they report a 2 km radar-bright spot located 8 km west of the center of the crater. It is particularly interesting to note that also VIMS detects a bright feature at the center of the crater, even if the spatial resolution of the VIMS images (14 km/pixel) is not sufficient to fully resolve this feature.

[23] Once reprojected, and considering the registration accuracy, the location of a bright area in the VIMS image is consistent with the bright spot identified in the SAR image (Figure 9). The feature might be the remains of a central peak, possibly partially buried under sediments or eroded. No significant spectral variation is observed in the spectrum of the central peak itself, suggesting that its constituting material, which has been excavated from a depth of up to

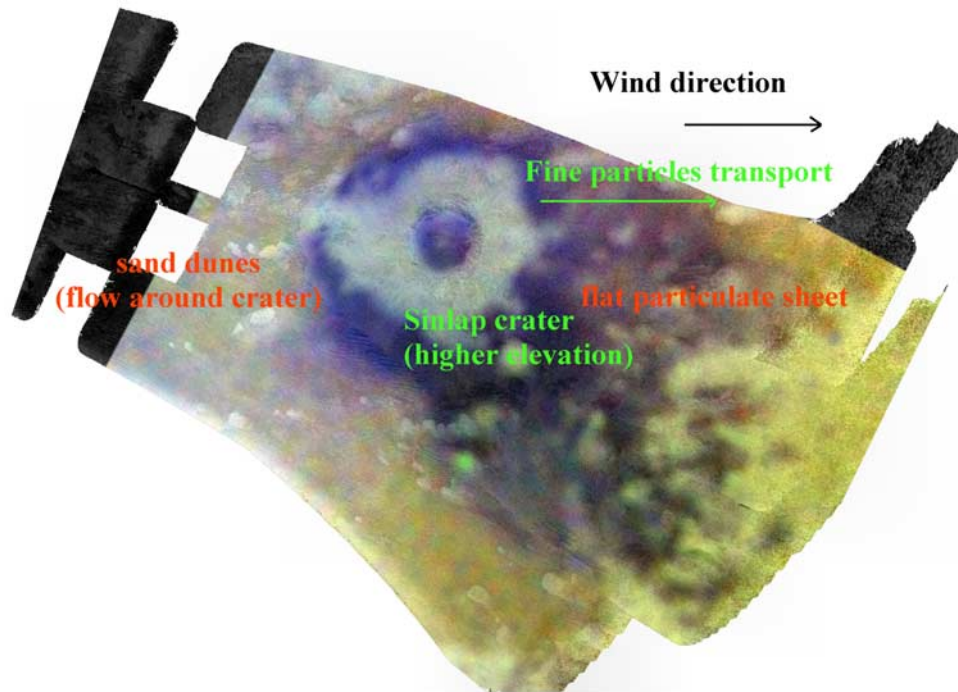


**Figure 7.** Labeled VIMS/RADAR mosaic of the Sinlap area. The colors are derived from VIMS T13 band ratios that are superimposed onto the T3 SAR image used as background. The dunes direction suggests the aeolian transport of light particles to the East.

10 km considering the size of Sinlap, does not differ markedly in composition from the bright surroundings. This suggests either that the impact target site was vertically homogeneous, or that the surface has been progressively recovered by thin homogeneous deposits after the impact. VIMS images of higher spatial resolution would be needed to go deeper into this analysis.

#### 4.3. A Spectrally Distinct Unit South of Sinlap?

[24] An anomalous area appears in green in the false color composite as shown in Figure 4. As already stated in section 2.4 (spectra discussion), this corresponds spatially to a single pixel, which has an anomalously high I/F value in the  $2\text{-}\mu\text{m}$  window as compared to other areas. Whereas it was observed in poorer conditions during the T5 flyby, the corresponding location (also falling in a single pixel) also exhibits a higher signal at  $2\text{ }\mu\text{m}$  than the surrounding pixels. The corresponding location in the SAR image corresponds to a shallow circular depression, at the border of the dune field (Figure 10). The stability of this point makes it noteworthy, but no definitive conclusion can be made on the exact nature of this terrain, and spectral data of higher spatial resolution than available now would also be needed to better constrain the variability of this site.

### 5. Comparison With Dielectric Constant Measurements Derived From Polarized Radiometric Data

[25] Passive microwave radiometry is obtained in all operational modes of the Ku-band (13.78 GHz, 2.18 cm) Cassini Titan Radar Mapper [Elachi *et al.*, 2005a]. The

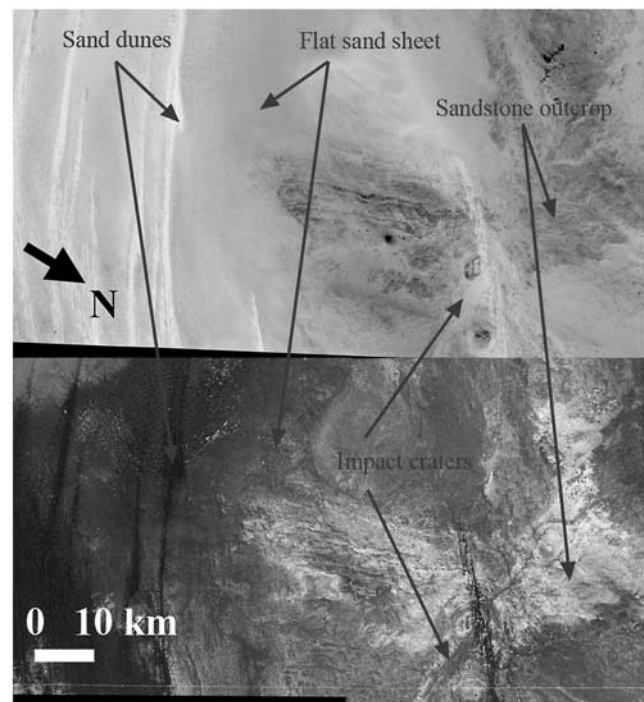


**Figure 8.** Earth analogue site in southern Libya. Top: Landsat ETM+ image at  $2.2\text{ }\mu\text{m}$ . Bottom: corresponding X-band (9.6 GHz) SAR image acquired during the 1994 SIR-C/X-SAR mission. The Landsat image shows a rather homogeneous sandy surface surrounding the outcropping relief, whereas the SAR image presents various structures due to the subsurface imaging capabilities of radar.

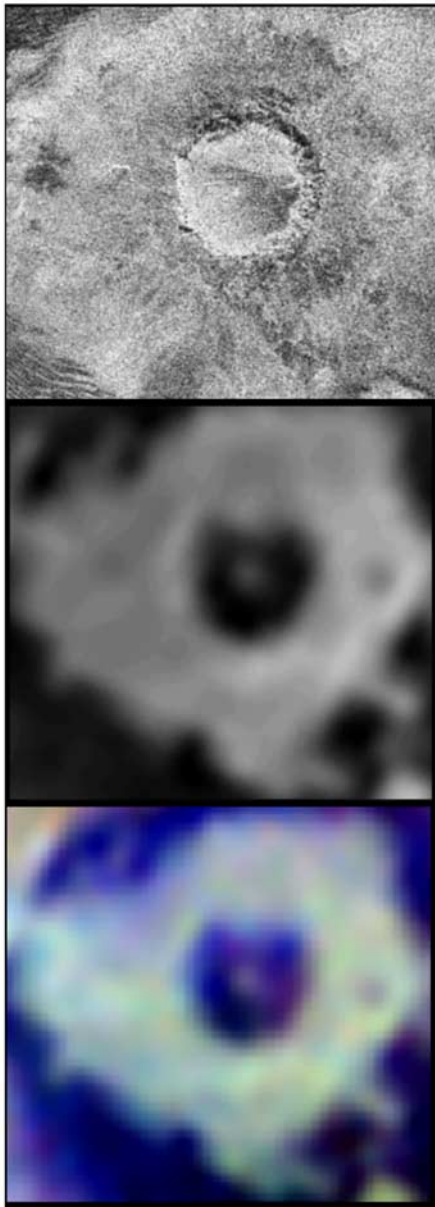


**Figure 9.** SAR image (top) and VIMS T13 ( $2\text{-}\mu\text{m}$  image in the middle and false color ratio composite at the bottom) images of the Sinlap crater, showing a possible central peak.

radiometric data are collected in one linear polarization using the main communications antenna of the spacecraft, which forms a circular beam of  $0.35^\circ$  half-power beam width in the central radar beam (beam 3). In the range approximately 30,000 to 100,000 km to Titan, there is sufficient time to image the thermal radiation from most of the disk twice by raster scanning, including a  $90^\circ$  rotation of the spacecraft to image in the orthogonal polarization. Spatial resolution at this distance from Titan is relatively low, ranging from 200 to 600 km on the surface of Titan. Closer to Titan the RADAR is typically operated in active mode, during which the radiometric data is obtained at higher spatial resolution although in only one sense of linear polarization. During SAR mode operations, the radiometric

data are obtained in all five radar beams, with a spatial resolution approaching 6 km in beam 3 at closest approach [Paganelli *et al.*, 2007].

[26] Thermal emission from a surface is polarized, and a measurement of the polarization can be used to infer the surface dielectric constant [Heiles and Drake, 1963]. The polarization is generally defined as the difference in brightness observed with the polarization in and orthogonal to the plane of incidence respectively, normalized by the sum. Hence it is independent of absolute calibration. For a surface that satisfies the Kirchhoff approximation (i.e., the wavelength is smaller than the characteristic dimensions of the surface), the surface dielectric constant can be obtained when the two senses of polarization are distinct with respect to the plane of incidence, and, while the emission angle must be sufficiently far from normal to obtain a measurable signal, it must not be so great that the interpretation is complicated by large-scale surface roughness effects. Only a fraction of the surface observed by the radiometer in orthogonal polarizations in any given pass meets these observing criteria; nevertheless, the dielectric constant has now been retrieved for most of Titan's surface using polarized data accumulated through the T30 pass [Janssen *et al.*, 2008]. As discussed by the authors, the dielectric model used holds only for uniform, homogeneous, and isotropic media interfaces, and must be interpreted with caution.

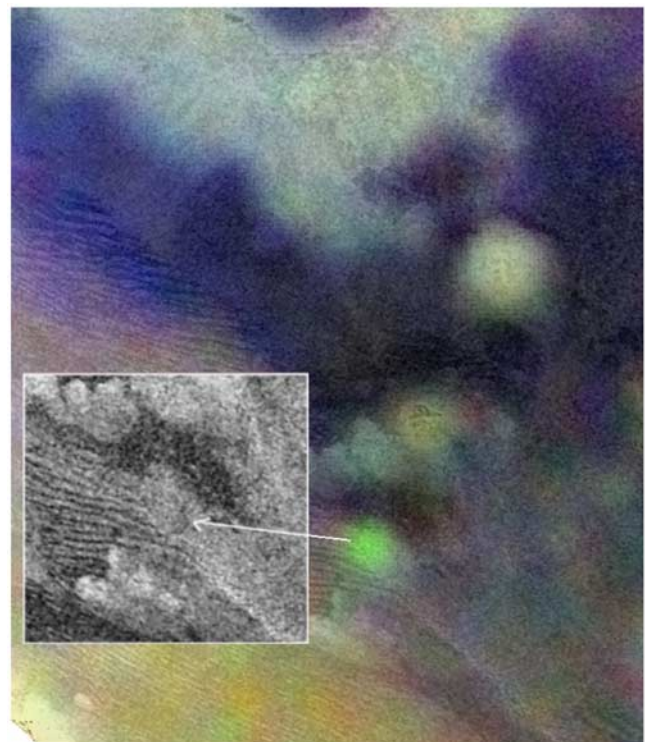


**Figure 10.** Anomalous area having a high reflectance at  $2.0\ \mu\text{m}$  and appearing with same spectral characteristics in T5 and T13 VIMS images. The corresponding location in the SAR image is a shallow depression at the edge of the dune field.

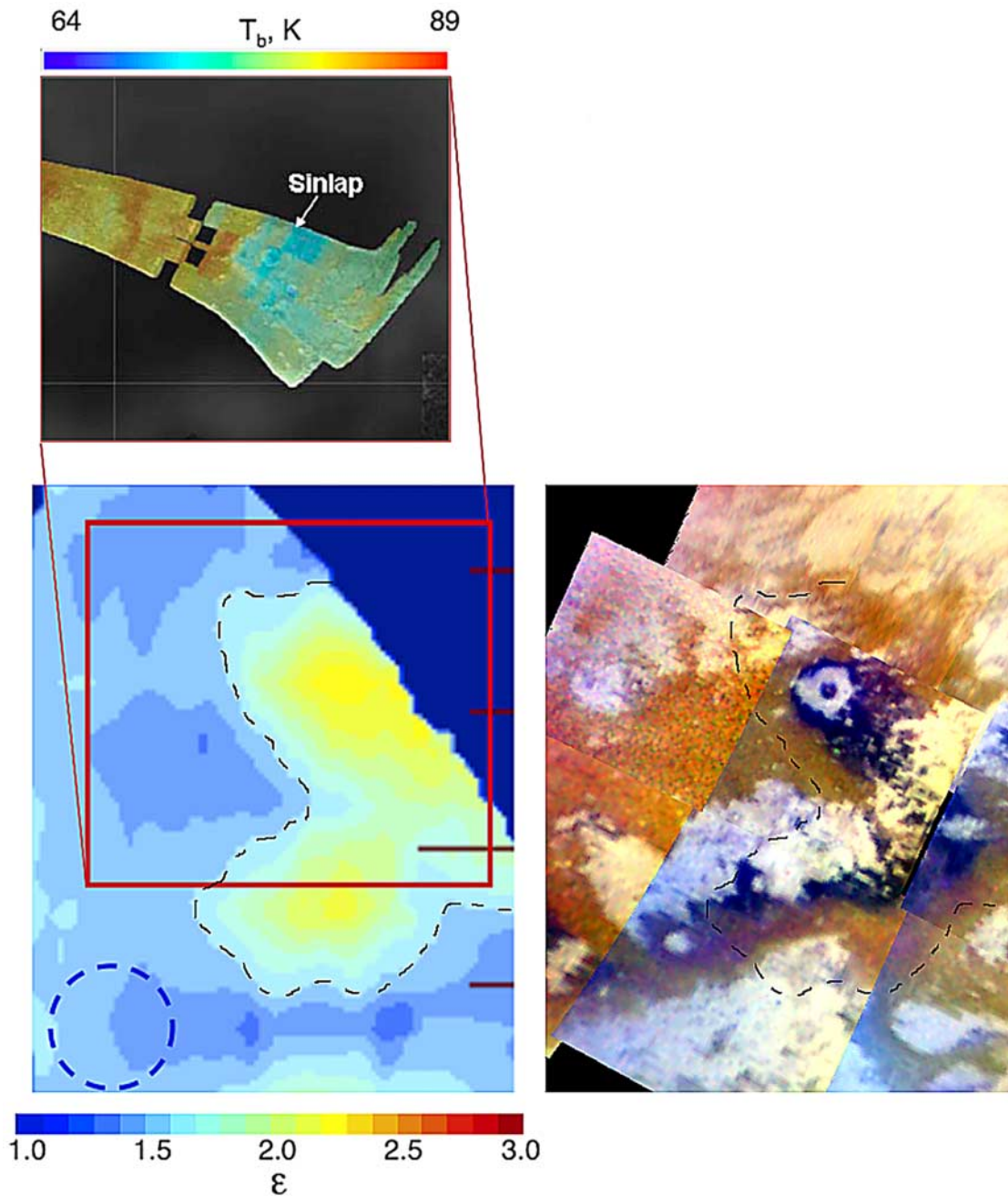


**Figure 11.** Top: The SAR image of Sinlap from T3 in black/white overlaid with a color map of radiometric brightness temperature obtained along with the SAR data [Paganelli *et al.*, 2007]. Bottom left: A portion of the dielectric constant map obtained from polarized radiometric data [Janssen *et al.*, 2008]. The red square indicates the area shown in the SAR map on the top. The dashed circle at the bottom left indicates the effective spatial resolution of the dielectric constant map (~500 km). Bottom right: VIMS false color ratio composite of T13 data (same color coding as in Figure 3f), where dark blue areas correspond to areas possibly enriched in water ice.

[27] Figure 11 shows a portion of the dielectric constant map that includes the Sinlap crater and its ejecta blanket, along with radiometry obtained on this region using the SAR mode at much higher spatial resolution (top). The data used to obtain the dielectric constant in this region were obtained during the outbound radiometry legs of the T8 and T19 passes. The SAR radiometry shows that the ejecta

blanket seen in the SAR map coincides with an area that is approximately 10 K cooler in terms of thermal emission as compared to its surroundings. Although only partially resolved at the ~500 km spatial resolution of the dielectric map (dashed circle in the lower left), the general region of the ejecta blanket coincides with a significant enhancement in dielectric constant. Another dielectric enhancement just

south of Sinlap coincides with a bright feature in Quivira region.

[28] The values for the dielectric constant retrieved from the polarized measurements are generally low, averaging about 1.6 across Titan. It is clear from the observation of many areas where the polarization is effectively zero (corresponding to a dielectric constant of unity) that the applicability of the Kirchhoff approximation on Titan is questionable in general. Nevertheless, the Sinlap feature is one of a few enhancements in dielectric constant that stand out across Titan [Janssen *et al.*, 2008] that begin to approach the value for water ice (3.1). However, the brightness deficit in the SAR image is too strong to be explained only by an increase in dielectric constant alone. Instead, it may further indicate that increased subsurface (volume) scattering may be present. The radiometric data as a whole are consistent with the interpretation of the region surrounding the Sinlap crater as a field that contains a significant fraction of exposed ice. This field is distinctly dissimilar to the surface of most of the rest of Titan and is probably of recent origin.

[29] It is also interesting to note that the second area appearing with a high dielectric constant in the Quivira region (south of Sinlap) correlates with materials also showing the same spectral characteristics as the Sinlap absorbing materials (the ones appearing in dark blue on the bottom right VIMS color composite of Figure 11). These areas can also be spectrally interpreted as having a higher content in water ice compared to the surroundings. As suggested for the settings of the materials in the Sinlap area, the particular spatial distribution of these surface materials, found only on the southern border of Quivira, might also be linked to the orientation of the dominant winds and to the transport of fine grained materials by these winds.

## 6. Geologic History

[30] As we have shown, Sinlap crater can play a critical role in helping us to understand the nature of Titan's surface. Sinlap is important not only because it is the largest crater, but rather because it is one of the best preserved, and therefore presumably one of the most recent craters on Titan. Sinlap displays many characteristics seen in no other of Titan's known craters or crater candidates: its well-preserved ejecta blanket, the parabolic dark blue halo, a possible central peak, and the surficial particulate sheet discussed in section 4 earlier. Presumably other Titanian craters have had these aspects at some point in their past, but erosion and post-impact geological evolution have contrived to subsequently remove them. As Titan's youngest known crater, Sinlap serves as an end-member for the wide variety of morphologies seen in craters and crater-candidates in various stages of degradation seen all over Titan. With the help of Sinlap's unique features, we therefore suggest a possible geologic history for Sinlap (Figure 12) with hopes of extrapolating back to what the lifecycle of a Titanian crater might be.

### 6.1. Pre-Impact

[31] There is no direct evidence for what the pre-impact surface was like at the Sinlap impact site. All of the features

that are associated with the crater overprint that former surface. However, given that the impact site is located within Titan's equatorial region and surrounded by sand dunes, we think it likely that the pre-impact surface at the Sinlap impact site was also part of the Fensal sand sea (Figure 12a). Extrapolating from T3 and T17 RADAR [Elachi *et al.*, 2006; Radebaugh *et al.*, 2007; Barnes *et al.*, 2008] and T20 high-resolution VIMS observations of dunes [Le Mouélic *et al.*, 2007; Barnes *et al.*, 2008] west of Sinlap, the pre-impact dune field might have similarly been composed of longitudinal dunes  $\sim 100$  km long and having crest-to-crest separations of 1–2 km [Radebaugh *et al.*, 2007].

[32] Based on theoretical arguments for Titan's crustal chemistry, Sinlap's pre-impact surface was likely predominantly water-ice or methane clathrate crust [Tobie *et al.*, 2006], with possibly a thin  $\sim 50$ –75 m equivalent thickness of dune material at the top. Whereas the bulk compositions of individual sand grains has not yet been established, VIMS spectra seem to indicate that the dunes are compositionally consistent with dark hydrocarbons (tholin-like material) and/or nitriles [Soderblom *et al.*, 2007], but they may represent a thin coating on predominantly icy grains.

### 6.2. Impact

[33] Assuming an icy impactor composition, and considering the crater size, the Sinlap-forming bolide had a diameter of 5 to 10 km with a presumed velocity ranging from 7 km/s to 15 km/s, and with an impact angle between 30 and 90 degrees [Artemieva and Lunine, 2003; Melosh and Beyer online impact calculator <http://www.lpl.arizona.edu/>]. It was large enough not to have been significantly decelerated by its passage through Titan's atmosphere [Artemieva and Lunine, 2003]. The impact came from an angle at least 10 degrees above the horizon, owing to the circularity of the crater rim, and symmetry of the proximal ejecta blanket.

[34] The impact vaporized target materials, and a fraction of the mass of the bolide [e.g., Artemieva and Lunine, 2005]. The heated vapor was injected into the atmosphere in an expanding plume. The composition of the plume was a function of the makeup of the impactor and target material. If Tobie *et al.* [2006] are correct, then the target materials vaporized may have been methane clathrate instead of pure ice. This hypothesis is interesting because in this case, the clathrates would have been dissociated during the impact, releasing methane into the atmosphere, and leaving a plume composed mainly of icy particulates which would recondense after the impact (Figure 12b).

[35] The impact delivered onto ballistic trajectories a large volume of ejecta, predominantly from the target crust. A continuous sheet surrounding the impact site was covered with ejecta. In addition to the continuous ejecta blanket, the impact also launched large blocks onto ballistic trajectories, as interpreted by Radebaugh *et al.* [2007]. These blocks would have created small mountain ranges upon landing.

### 6.3. Immediately Post-Impact

[36] The expanding plume of vapor from the impact expands until its internal pressure matches that of the surrounding atmosphere (Figure 12b). For an impact of

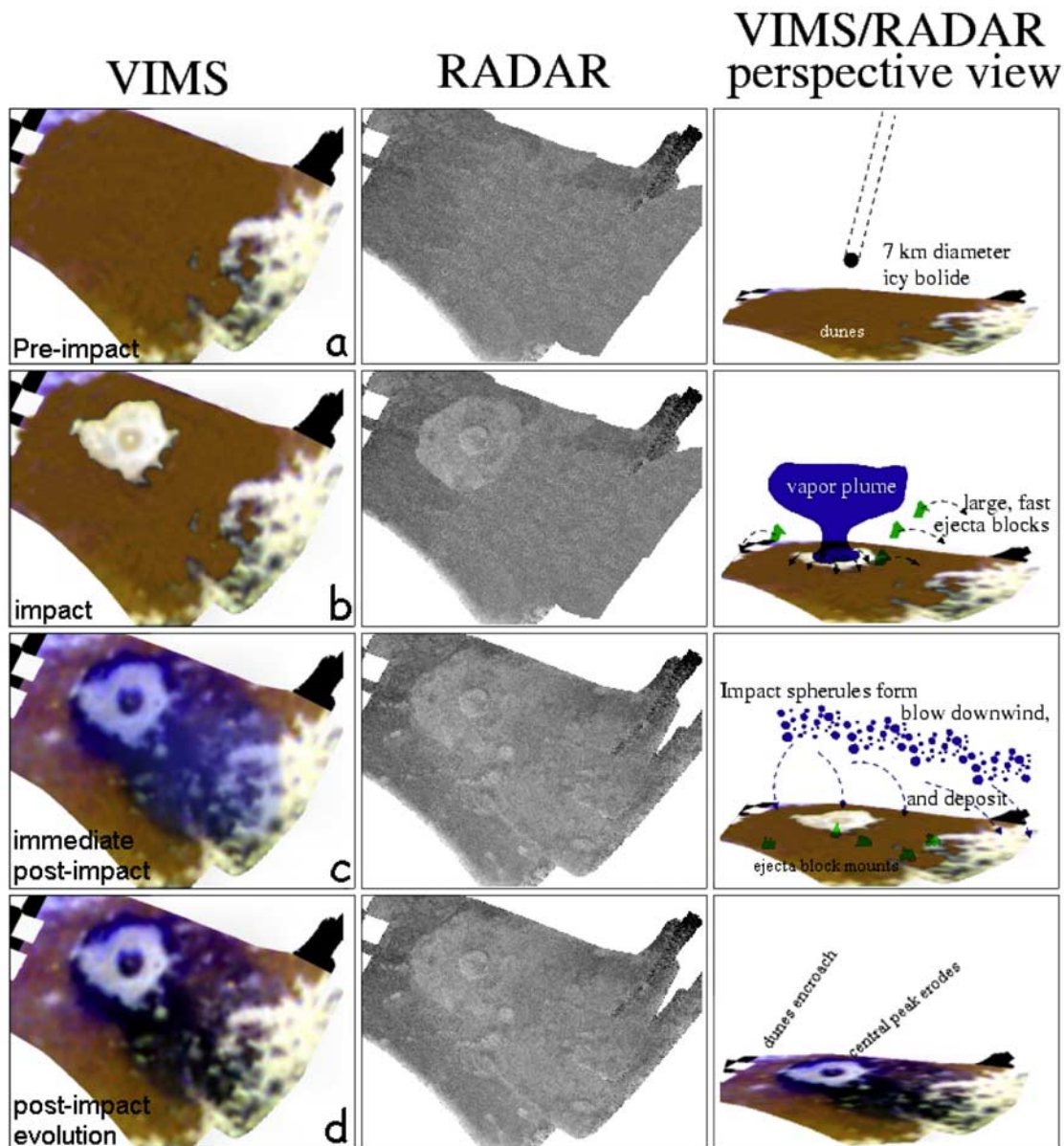


**Figure 12.** Proposed formation scenario for Sinlap. (a) Pre-impact site corresponding to Fensal sand sea. (b) Impact by a  $\sim 7$  km body creating ballistic ejecta and vapor plume. (c) Recondensation and deposition of the vapor plume blown downwind. (d) Current situation.

sufficient size, the plume expands to a size comparable to or larger than the scale height of the planet's atmosphere, in which case it cannot reach pressure equilibrium and instead blows the top off of the atmosphere, distributing ejecta over a much broader area [Melosh, 1989, p. 212]. Such a piercing of the atmosphere has been implicated in the formation of parabolic ejecta blankets surrounding Venusian craters [Vervack and Melosh, 1992; Schaller and Melosh, 1998]. The Venusian impact parabolae were discovered using 12.6 cm synthetic aperture radar from the Magellan spacecraft. They are radar-dark, and inferred to be smooth, at the Magellan wavelengths, and extend westward from the source craters that are present near the parabolae's foci, consistent with Venus' global wind patterns blowing material downwind. Sinlap's parabola is noteworthy, as mentioned above, in that it does not readily appear in the Cassini

2.2 cm SAR imaging, but is evident in shorter-wavelength infrared reflection as seen by VIMS. Sinlap's parabola extends East-South-East from the source crater; the west-to-east wind pattern implied by the parabola's orientation is consistent with that inferred from sand dune orientations and morphology [Lorenz *et al.*, 2006]. As the dark blue, icy parabola associated with Sinlap qualitatively resembles those found surrounding Venusian craters, we investigate whether the Sinlap parabola might have formed similarly. In this paper we merely calculate the feasibility of similar formation mechanisms, leaving more complete computational modeling to future work.

[37] Following Vervack and Melosh [1992] then, who in turn followed Melosh [1989] and Jones and Kodis [1982], we calculate the minimum radius necessary for a cometary-composition impactor to blow out the atmo-

sphere when impacting into Titan. The minimum impactor radius,  $a_p$ , is:

$$a_p = H(P_0/S\rho_p v_i^2)^{1/3\gamma},$$

where  $H$  is the atmospheric scale height (55 km; inferred from *Fulchignoni et al.* [2005] Figure 4),  $P_0$  is the ambient surface atmospheric pressure (146.7 kPa from *Fulchignoni et al.* [2005]),  $S$  is a constant from the linear shock-particle velocity equation of state (equal to 1.56 for ice; e.g., *Melosh* [1989]),  $\rho_p$  is the impactor's density (assumed to be  $0.91 \text{ g}\cdot\text{cm}^{-3}$  as for pure water ice),  $v_i$  is the impactor velocity (taken as 11.5 km/s for a heliocentric impactor), and  $\gamma$  is the ratio of specific heats (assumed to be 1.4 for  $\text{N}_2$ ). Using these values,  $a_p$  should be about 2 kilometers. The Sinlap bolide, at 5 to 10 km diameter depending on its origin, was therefore large enough to have blown the top of the atmosphere on impact, like those Venusian impactors that created craters with parabolic ejecta.

[38] Once outside the atmosphere, the recondensed icy impact spherules travel on ballistic trajectories until they re-encounter the atmosphere on the way down. At this point they continue to fall through the atmosphere at their terminal velocity, moving with the local winds (Figure 12c). *Vervack and Meloch* [1992] show that smaller plume-entrained ejecta particles have higher initial velocities, which leads them to travel further from the crater ballistically. Those smaller particles also have lower terminal velocities, leading them to fall further downwind from the source crater, and driving the ejecta pattern's parabolic shape.

[39] Sinlap's parabola dimensions differ in proportion to those on Venus. The Venusian parabolas have a broader opening angle than Sinlap's, and are much larger for a given crater size. Crater Stowe on Venus, at 82 km diameter similar to Sinlap, has a parabola with a total length and width of 1520 and 1320 km, respectively, several times the area of Sinlap. Detailed modeling is required to determine the parameters driving these differences, which we leave to future work. The orientation of the parabolae on Venus, all either open toward the west or nearly circular, has been attributed to Venus' east-to-west global wind pattern. Falling ejecta particles drift with the surrounding atmosphere while they fall at terminal velocity; hence the orientation of the resulting parabola should be a strong function of the winds at altitude, and not that of surface winds. On the basis of the orientation of Sinlap's parabola, we infer that the average wind direction, at altitude, in Sinlap's location at the time of the impact was from  $\sim 30$  degrees north of west. This west-to-east atmospheric flow is consistent with the superrotating atmosphere measured by the Huygens probe as it descended [*Bird et al.*, 2005]. It is also roughly consistent with Huygens Descent Imager Spectral Radiometer (DISR) imaging of the probe's ground track. DISR showed a consistent west-to-east motion through the descent until the probe dropped to an altitude of 7 km, whereby which the winds reversed, becoming east-to-west [*Tomasko et al.*, 2005]. This is consistent with our determination in that the spatial distribution of falling impact ejecta is dominated by the average atmospheric winds, not by those at the surface.

[40] Assuming a predominantly icy composition for the first kilometers of Titan's crust, the deposited plume mate-

rial would also be mostly water-ice. The ejecta deposits should have covered everything within the parabola, including the impact site itself. Hence we speculate that after the impact, the Sinlap site might have looked something like Figure 12c, with bright blue material covering the parabola.

[41] In this scenario, the plume blown downwind (and having a parabolic shape once deposited on the ground) would display enriched water ice absorption features compared to the surroundings. It would also represent only a thin coating, consistent with the difference observed between VIMS and RADAR images, as discussed previously.

#### 6.4. Post-Impact Evolution to Present-Day

[42] The current situation might well be a combination of several processes such as the settings of the main ejecta blanket as discussed previously, the redeposition of an icy vapor plume blown downwind, and subsequent evolution driven by erosional processes and aeolian deposition, which might be active since the impact occurred.

[43] With a few exceptions (notably Xanadu), bright areas within 25 degrees of Titan's equator all have similar spectral character [*McCord et al.*, 2006; *Soderblom et al.*, 2007; *Barnes et al.*, 2007]. Sinlap's nearby ejecta blanket, the bright area Bazaruto Facula as seen in the infrared, shows no spectral digressions from any of the rest of the equatorial bright material. This, in itself, is remarkable: a feature known to be relatively young that nevertheless looks the same as much older terrains.

[44] Sinlap's dark blue parabola is unique in that it is the only instance of dark blue terrain discovered so far that does not lie only on a single side of a bright area (supposed to be of higher topography). For example, dark blue terrains are found only on the southern side of Quivira (Figure 11), whereas it is found almost all around Sinlap's Barazuto Facula. *Barnes et al.* [2007] proposed that dark blue terrain is composed of outwash from the similarly dark blue channels, but that such outwash is covered up by blowing sand dune material in those places the wind can access. The Sinlap parabola is apparently inconsistent with this view in that there are no visible nearby channels to have produced it and in that it is also open to the east, and hence should be fully covered by sand dunes.

[45] We therefore propose a scenario for the post-impact geological evolution of the Sinlap area that is consistent with both VIMS data for Bazaruto Facula and the Sinlap parabola, and RADAR observations.

[46] The (presumably) initially VIMS bright blue, icy impact spherules that formed Sinlap's parabola were chemically processed into VIMS dark blue material. Similar transformations clearly occur to produce the dark blue channel-bottoms seen by VIMS [*Barnes et al.*, 2007], but are not yet understood

[47] Rain erosion washed the dark blue spherules off of high-lying Bazaruto Facula into neighboring low-lying regions. Hence the outer portion of the local Sinlap ejecta blanket seen by RADAR could be covered in VIMS dark blue spherules washed from Bazaruto Facula.

[48] The crater bowl was filled in by icy bedrock that eroded from the crater rim and impact spherules that washed or blew in by methane rainfall or wind, covering the underlying melt sheet. Similar effects are seen in Earth's best preserved crater, Barringer Crater in Arizona, which

has its floor covered by tens of meters of lakebed sediments laid down in cooler climate during the last glaciation [Masaitis, 2006].

[49] The central peak was eroded downward, and its flanks covered up by sediments. The remaining central patch seen by VIMS represents vestigial high terrain around the location of what once would have been a much-higher central peak.

[50] Sand dunes marched across the ejecta west-to-east (Figure 12d), partially covering proximal ejecta as seen by RADAR. The finest fractions of the sand were transported from the dune field across the crater to form a thin deposit on the eastern part of the ejecta blanket.

### 6.5. Future Evolution

[51] Though few craters on Titan have been unambiguously identified, many suspiciously circular features have been seen by RADAR, ISS, and VIMS that may represent older impact scars in various stages of degradation. On the basis of these possibly older craters, we speculatively project what the future geologic evolution of the Sinlap area might be like. The longitudinal dunes that are presently encroaching on Bazaruto Facula are likely to continue to do so. Dune encroachment also depends on simultaneous erosion of highstanding features. There are many high features that dunes appear unable to climb, so they probably need to "wait" until erosion brings features down low enough for them to cover. 1.5 km elevations as measured by the RADAR are relatively rare on Titan. In the near-future, Sinlap and its ejecta blanket will probably grow to resemble the 30 km Ksa crater [Lorenz *et al.*, 2007]. Given much more time, the dunes could cover the entire ejecta blanket and crater bowl, creating a feature that more resembles Guabonito Facula [Porco *et al.*, 2005]. Divining the future of Sinlap's ejecta parabola is more challenging, as it is unique on present-day Titan. We speculate that Sinlap's parabola should be relatively long-lived in that some remnant of it should exist until the dunes completely overtake it or until it itself is eroded into other surface units.

## 7. Conclusion and Perspectives

[52] Among the 44 flybys of Titan planned for the nominal Cassini-Huygens mission, 35 flybys have been performed so far. Only very few impact craters (or circular features possibly related to impact processes) have been observed, which indicates that the surface of Titan is geologically young [Elachi *et al.*, 2005b; Porco *et al.*, 2005; Lorenz *et al.*, 2007]. Among these identified features, Sinlap is the only case of a well preserved crater where we have both VIMS coverage at medium resolution and high-resolution SAR imagery. Interesting correlations can be observed between the spectrally distinct areas identified in the infrared data and the SAR image. Dark areas surrounding the Sinlap region in VIMS imagery (and appearing in brown in the color ratio composites) correspond to dune fields as seen in the SAR image. Several units can be identified in the crater region. The dark (in infrared) crater floor corresponds to the unit delimited by the crater rim in the SAR image, with possibly a central peak identified in both. The bright circular ejecta pattern in

VIMS corresponds to moderately bright materials in the radar showing a specific texture and radial patterns. The VIMS false infrared color composites reveal a spectrally distinct unit with a parabolic shape surrounding the main bright crater unit, and appearing in bluish to dark in the false color ratio images.

[53] This dark bluish parabolic area has a distinct spectral behavior which can be explained by a possible enrichment in water ice as compared to its surroundings. Measurements of the dielectric constant performed at a low spatial resolution by using polarized radiometric data also support an enrichment in water ice in this region. Furthermore, this area also correlates well with high radar backscatter intensity values. This can be explained by considering the difference in penetration depth of the infrared and radar wavelengths. The radar might see the bedrock through a thin layer deposit. This interpretation is supported by infrared Landsat and SAR imagery of a terrestrial analogue site in Libya, showing sand sheet covers over impact craters. On Sinlap, this layer may have been emplaced by the immediate post-impact vapor plume, and modified by subsequent wind transportation and erosional processes.

[54] The correlation between infrared and radar features is not systematic, and differences can be explained considering the different sensitivities of both instruments with respect to surface composition and roughness, and also the sub-surface imaging capabilities of the SAR instrument. The two data sets provide very complementary information about surface properties. It would be of high interest to study the most interesting geological features on Titan with both VIMS and RADAR instruments, in order to constrain the processes which led to their formation by analyzing both surface and sub-surface features. The spatial resolution of VIMS images can be as good as 500 m per pixel when observing during the closest approach. This was done for the first time during the T20 flyby. This resolution is similar to the resolution of the SAR images, and allowed for example to resolve for the first time the dunes in the infrared [e.g., Le Mouélic *et al.*, 2007; Barnes *et al.*, 2008]. However, considering the orbital constraints, no observation of Sinlap will be performed with VIMS at such a resolution (and none better than 5 km/pixel) during the nominal Cassini mission. It could be very interesting to acquire such a new data set in the future, in order to go deeper into the analysis of this impact feature and other crater candidates. New well preserved impact craters may also be discovered considering the increasing spatial coverage of Cassini imaging instruments, allowing more comparison between VIMS (high resolution) and RADAR images.

[55] **Acknowledgments.** Authors are very grateful to Jani Radebaugh and an anonymous reviewer for their insightful and thorough reviews which greatly improved this paper. Thanks to the VIMS and RADAR science and implementation teams for getting the data. This work has been partly funded by the French spatial agency (CNES). It has been carried out when C. Sotin was distinguished visiting scientist at the Jet Propulsion Laboratory/Caltech.

## References

- Artemieva, N., and J. I. Lunine (2003), Cratering on Titan: Impact melt, ejecta, and the fate of surface organics, *Icarus*, 164, 471–480.
- Artemieva, N., and J. I. Lunine (2005), Impact cratering on Titan II. Global melt, escaping ejecta, and aqueous alteration of surface organics, *Icarus*, 175, 522–533.

- Barnes, J. W., et al. (2005), A 5 micron bright spot on Titan: Evidence for surface diversity, *Science*, *310*, 92–95, doi:10.1126/science.1117075.
- Barnes, J. W., et al. (2006a), Cassini observations of flow-like features in western Tui region, Titan, *Geophys. Res. Lett.*, *33*, L16204, doi:10.1029/2006GL026843.
- Barnes, J. W., et al. (2006b), Global-scale surface spectral variations on Titan seen from Cassini/VIMS, *Icarus*, *186*, 242–258, doi:10.1016/j.icarus.2006.08.021.
- Barnes, J. W., et al. (2007), Near infrared spectral mapping of Titan's Mountains and channels, *J. Geophys. Res.*, *112*, E11006, doi:10.1029/2007JE002932.
- Barnes, J. W., et al. (2008), Spectroscopy, morphometry, and photoclinometry of Titan's dunefields from Cassini/VIMS, *Icarus*, in press, available online 3 Jan.
- Bird, et al. (2005), The vertical profile of winds on Titan, *Nature*, *438*(7069), 800–802.
- Brown, R. H., et al. (2003), Observations with the Visual and Infrared Mapping Spectrometer (VIMS) during Cassini's flyby of Jupiter, *Icarus*, *164*, 461–470.
- Brown, R. H., et al. (2004), The Cassini Visual and Infrared Mapping Spectrometer (VIMS) investigation, *Space Sci. Rev.*, *115*, 111–168, doi:10.1007/s11214-004-1453-x.
- Elachi, C., L. E. Roth, and G. G. Schaber (1984), Spaceborne radar subsurface imaging in hyperarid regions, *IEEE Trans. Geosci. Remote Sens.*, *GE-22*, 383–388.
- Elachi, C., et al. (2005a), RADAR: The Cassini Titan radar mapper, *Space Sci. Rev.*, *117*, 71–110.
- Elachi, C., et al. (2005b), Cassini radarviews the surface of Titan, *Science*, *308*, 970–974.
- Elachi, C., et al. (2006), Titan radar mapper observations from Cassini's T3 fly-by, *Nature*, *441*, doi:10.1038/nature04786.
- Fulchignoni, et al. (2005), In situ measurements of the physical characteristics of Titan's environment, *Nature*, *438*, 787–791.
- Heiles, C. E., and F. D. Drake (1963), The polarization and intensity of thermal radiation from a planetary surface, *Icarus*, *2*, 281–292.
- Janssen, M. A., et al. (2008), Titan's surface at 2.2-cm wavelength as imaged by the Cassini RADAR radiometer: Calibration and first results, *Icarus*, in prep.
- Jones, E. M., and J. W. Kodis (1982), Gradient acceleration as a mechanism for rapid worldwide dispersal of particulates following a large-body impact, *Lunar Planet. Sci.*, *XIII*, 367–368.
- Le Mouélic, S., et al. (2007), Spatial and spectral filtering strategies for Cassini VIMS surface images of Titan, *38th Annual Lunar and Planetary Science Conference*, March 12–16, League City, abstract 1574.
- Lorenz, R. D., et al. (2006), The sand seas of Titan: Cassini RADAR observations of longitudinal dunes, *Science*, *312*, 724–727, doi:10.1126/science.1123257.
- Lorenz, R. D., et al. (2007), Titan's young surface: Initial impact crater survey by Cassini RADAR and model comparison, *Geophys. Res. Lett.*, *34*(7), L07204, doi:10.1029/2006GL028971.
- Masaitis, V. L. (2006), Review of the Barringer crater studies and views on the crater's origin, *Sol. Syst. Res.*, *40*(6), 500–512.
- McCord, T. B., et al. (2006), Composition of Titan's surface from Cassini VIMS, *Planet. Space Sci.*, *54*, 1524–1539.
- Melosh, H. J. (1989), *Impact cratering: A Geologic process*, Oxford Univ. Press, New York. 245 p.
- Paganelli, F., et al. (2007), Titan's surface from the Cassini Radar SAR and high-resolution radiometry data of the first five flybys, *Icarus*, doi:10.1016/j.icarus.2007.04.032.
- Paillou, Ph., A. Rosenqvist, J.-M. Malézieux, B. Reynard, T. Farr, and E. Heggy (2003), Discovery of a double impact crater in Libya: The astrobleme of Arkenu, *C. R. Acad. Sci. Paris, Geosci.*, *335*, 1059–1069.
- Paillou, Ph., M. Crapeau, S. Wall, Ch. Elachi, and P. Encrenaz (2006), Models of SAR backscattering for bright flows and dark spots on Titan, *J. Geophys. Res.*, *111*, E11011, doi:10.1029/2006JE002724.
- Perry, J. E., A. S. McEwen, S. Fussner, E. P. Turtle, R. A. West, C. C. Porco, B. Knowles, and D. D. Dawson (2005), The Cassini ISS team, processing ISS images of Titan's surface, *36th Annual Lunar and Planetary Science Conference*, March 14–18, 2005, League City, Texas, abstract 2312.
- Porco, C., et al. (2005), Imaging of Titan from the Cassini spacecraft, *Nature*, *434*(7030), 159–168.
- Radebaugh, J., et al. (2007), Dunes on Titan observed by Cassini Radar, *Icarus*, in press, available online 21 Nov.
- Rannou, P., F. Montmessin, F. Hourdin, and S. Lebonnois (2006), The latitudinal distribution of clouds on Titan, *Science*, *311*, 201–205.
- Rodriguez, S., S. Le Mouélic, C. Sotin, H. Clénet, R. N. Clark, B. Buratti, R. H. Brown, T. B. McCord, P. D. Nicholson, K. H. Baines, and the VIMS Science Team (2006), Cassini/VIMS hyperspectral observations of the Huygens landing site on Titan, *Planet. Space Sci.*, *54*, 1510–1523.
- Schaller, C. J., and H. J. Melosh (1998), Venusian ejecta parabolas: Comparing theory with observations, *Icarus*, *131*, 123–137.
- Soderblom, L., et al. (2007), Correlations between Cassini VIMS spectra and RADAR SAR Images: Implications for Titan's surface composition and the character of the Huygens Probe landing site, *Planet. Space Sci.*, Published online 2007 April 27.
- Sotin, C., et al. (2005), Release of volatiles from a possible cryovolcano from near-infrared imaging of Titan, *Nature*, *435*, 786–789, doi:10.1038/nature03596.
- Tobie, G., J. Lunine, and C. Sotin (2006), Episodic outgassing as the origin of atmospheric methane on Titan, *Nature*, *440*(7080), 61–64.
- Tomasko, M. G., et al. (2005), Rain, winds and haze during the Huygens probe's descent to Titan's surface, *Nature*, *438*(7069), 765–778.
- Vervack, R. J., Jr., and H. J. Melosh (1992), Wind interaction with falling ejecta – Origin of the parabolic features on Venus, *Geophys. Res. Lett.*, *19*, 525–528.

K. H. Baines, B. J. Buratti, M. A. Janssen, F. Paganelli, C. Sotin, and S. Wall, Jet Propulsion Laboratory, M/S 183-501, 4800 Oak Grove Drive, Pasadena, CA 91109, USA.

J. W. Barnes, NASA Ames Research Center, M/S 244-30, Moffett Field, CA 94035, USA.

R. H. Brown, Lunar and Planetary Lab, University of Arizona, Tucson, AZ 85721, USA.

R. N. Clark, USGS, Denver, CO 80225, USA.

M. Crapeau and P. Paillou, Observatoire Aquitain des Sciences de l'Univers-UMR 5804, Floirac, France.

P. J. Encrenaz, Observatoire de Paris/Université Pierre et Marie Curie, 61 Avenue de l'Observatoire 75014, Paris, France.

D. Geudtner, German Aerospace Center, Microwave and Radar Institute, Germany/Canadian Space Agency, Spacecraft Payloads, Canada.

R. Jaumann, DLR, Institute for Planetary Research, Berlin, Germany.

S. Le Mouélic and G. Tobie, Université de Nantes, Laboratoire de Planétologie et Géodynamique, 2 rue Houssinière, 44322 Nantes Cedex 03, France. (stephane.lemouelic@univ-nantes.fr)

S. Rodriguez, Université Paris 7, Laboratoire AIM, Centre d'étude de Saclay, DAPNIA/Sap, Centre de l'Orme des Merisiers, bât. 709, France.

L. Soderblom, USGS, Flagstaff, AZ 86001, USA.